Numerical Simulations of Carbon Contaminants in T6 Shock Tube Tests

Justin Clarke *, Alex Glenn †, Orin Varley ‡, Luca Di Mare § and Matthew McGilvray ¶
University of Oxford, Oxford, OX1 2JD, United Kingdom

The influence of carbon contamination on a range of synthetic air and pure nitrogen shock tube experiments conducted in Oxford's T6 Stalker Tunnel is investigated using a numerical model designed for thermochemically reacting flows. Experimental conditions range from 6 to 7 km/s with fill pressures between 18 and 100 Pa. The addition of carbon was found to significantly improve agreement between the numerical model and experimental data, especially after the non-equilibrium peak and during relaxation towards equilibrium. For the chosen thermochemistry set and test conditions, minimal affect on the chemical kinetics of the original test gas was found especially for the neutral species, with minor changes for ion and electron number densities. The performance of the chosen thermochemistry model in radiance regions corresponding to NO and non-equilibrium atomic oxygen was poor, with improvements also required for the parameters governing translational-vibrational relaxation.

Nomenclature

A_{ij}	=	Millikan-White constant for interactions between species i and j
b_{ij}	=	Millikan-White constant for interactions between species i and j
C	=	Coefficient for forward reaction rate in the Arrhenius equation
n	=	Coefficient for forward reaction rate in the Arrhenius equation
P	=	Pressure (Pa)
T_a	=	Average temperature $\sqrt{T_t T_v}$ (K)
T_e	=	Electronic temperature (K)
T_E	=	Activation temperature (K)
T_r	=	Rotational temperature (K)
T_t	=	Translational temperature (K)
T_v	=	Vibrational temperature (K)
σ_v	=	Effective cross section for vibrational relaxation (m^2)
$\tau_{MW,ij}$	=	Millikan-White translational-vibrational relaxation time for interactions between species i and j
θ_i	=	Characteristic temperature for species i (K)
μ_{ij}	=	Reduced mass between species i and j

I. Introduction

Non-equilibrium phenomena can notably influence the aerothermodynamic characteristics, encompassing heat transfer and radiative transport properties, of vehicles as they enter planetary atmospheres. The design of vehicles intended for entry into these atmospheres heavily relies on numerical calculations, demanding accurate estimations of physical quantities such as reaction rate constants and intra-molecular interaction parameters. The numerical predictions of hypersonic flows crucially depend on obtaining reliable data for reaction rate constants and intra-molecular parameters related to transport quantities. This data is drawn from a diverse array of sources [1]. However, the flow conditions typically encountered during planetary entry are impractical to replicate in continuous flow facilities due to their extreme power requirements. Consequently, the study of such conditions necessitates the utilization of shock tube facilities.

*D.Phil. Candidate, Department of Engineering Science, Osney Thermofluids Institute.
†D.Phil. Candidate, Department of Engineering Science, Osney Thermofluids Institute.
‡Post-doctoral Researcher, Department of Engineering Science, Osney Thermofluids Institute.
§Associate Professor, Department of Engineering Science, Osney Thermofluids Institute.
¶Professor, Department of Engineering Science, Osney Thermofluids Institute.

Shock tube facilities utilize a high-pressure, high sound-speed driver to transmit a shock wave through a tube containing the test gas, which produces the desired flow conditions [2]. Various flow non-uniformities arise due to the unique processes during these experiments, encompassing effects from driver operation [3], diaphragm rupture [4, 5], and boundary layer effects [6]. These processes govern the spatial and temporal variations in the properties of the test gas. Consequently, appropriately characterizing the test gas state in a shock tube becomes a challenging task. Full facility simulations encounter limitations in predicting these non-uniformities, attributed to experimental variations in initial fill conditions, contaminants, and rupture conditions. This challenge is exacerbated by the computational cost of adequately resolving the shock as it traverses the extended tube [7]. Consequently, when analyzing shock tube spectroscopy data, assumptions and simplifications regarding flow patterns or distributions of gas properties become necessary. For instance, when determining rate coefficients for high-temperature reactions from spectroscopic data generated by shock tubes [8–11], assumptions about the temperature and pressure profiles of the test gas behind the shock are imperative.

Recent experimental campaigns have been undertaken at Oxford to investigate the behaviour of synthetic air and nitrogen in shocks ranging from 6-8 km/s [12]. These experiments produced results which indicate the presence of contaminants in the flow, specifically carbonaceous species such as cyanogen (CN). These contaminants have been observed in many other experimental groups [13–15]. These carbon species are typically slower reacting than those associated with synthetic air [16], and as such require accurate modelling of the fluid dynamics present in a shock tube to allow comparison of numerical results to experimental datasets [17]. Previous work has not modelled the affect of low level contamination on shock tube data, however carbon species at higher levels have been modelled using blunt body models to compare against shock tube tests relevant for Titan and Martian entry [16, 18].

In this paper, we will utilise a numerical tool specifically developed for appropriately modelling shock tube flow coupled with a fully reacting thermochemistry model. By adding low level of carbon contaminants, we can analyse the influence of carbonaceous products on the chemical kinetics and hence expected radiance, and also evaluate the performance of the specified thermochemistry model.

II. Experiments

The University of Oxford T6 Stalker Tunnel is a multi-mode shock tube utilising a free-piston driver to perform high-enthalpy hypersonic experiments. T6 was operated in the aluminium shock tube (AST) mode of operation in the experiments considered, AST has been extensively described [2, 19]. The AST has a conical expansion from 96.3 to 225mm after the secondary driver (see Figure 1), with 6m separating the end of the conical expansion to the viewing window of the spectroscopy equipment. Each test utilised two spectroscopy cameras, one measuring in the

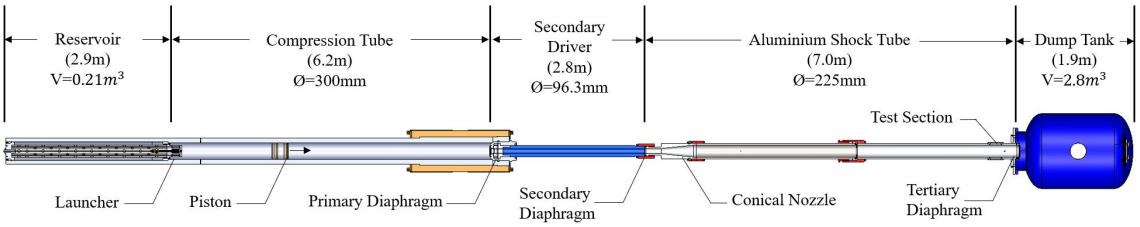

Fig. 1 Section view of the T6 shock tunnel in AST mode. Image from [15].

visible/ultraviolet region and the other measuring in the visible/near infrared region. The experimental setup used specifically in these tests is described comprehensively by Glenn et al. [12] Spatial resolution functions (SRF) and instrument line shapes (ILS) were determined by Glenn et al. for each test, allowing numerical results to be convolved spectrally and spatially for direct comparison to experimental data.

A. Tests Overview

Of the tests undertaken in the campaign by Glenn et al., seven were chosen for analysis. Shock speeds range from 6.1 km/s to 7.3 km/s, and fill pressures range from 18 Pa to 105 Pa. Each synthetic air (71% N_2, 21% O_2 by volume) condition has an equivalent pure nitrogen test. Shots were chosen for their relatively constant shock trajectory, minimising the influence of shock variation on the test slug [20, 21]. An overview of shot conditions are shown in Table 1. The value of the maximal Mirels' length is evaluated assuming post-shock equilibrium values using Mirels [22],

these values are all significantly longer than the 100 mm window used when obtaining the spectroscopy images.

Table 1 T6 shot conditions chosen for analysis from Glenn et al. [12]

Test No.	Shock speed (m/s)	Fill pressure (Pa)	Gas comp. by volume	Mirels length (m)
T6s482	6200	107.541	100% N_2	3.035
T6s478	6100	105.132	79% N_2, 21% O_2	2.88
T6s493	7050	33.755	100% N_2	0.88
T6s484	7300	33.287	79%N_2, 21% O_2	0.839
T6s501	7250	33.287	79% N_2, 21% O_2	0.839
T6s495	7250	18.235	100% N_2	0.473
T6s491	7250	18.034	79% N_2, 21% O_2	0.454

III. Modelling Approach

The numerical modelling approach utilised for analysis of the chosen shock tube tests can be broken into three separate components:

- Fluid dynamics solver for modelling reacting shock tube flow
- Thermochemistry model
- Radiance model

This allows the unique hydrodynamics present in a shock tube to be appropriately modelled such that the chosen reacting gas thermochemistry model produces spatially accurate state properties [17, 23], allowing for an appropriate estimation of expected radiance.

To model the influence of carbon contaminants present during tests, C_2 is added to the fill composition of the test gas. The C_2 volume fraction is chosen such that the radiance profile between 360nm and 290nm agrees with the experimental profile for a nominated distance in the post-shock region (approximately 6-7cm post-shock in most tests). This corresponds to a wavelength region where CN radiation has the most significant contribution to the overall radiance profile. The chosen levels of C_2 contamination by volume is shown in Table III. All contaminants are orders of magnitudes lower than the primary species present, and are of a magnitude feasible due to a combination of wall contamination, outgassing and leakage prior to the shot firing.

Table 2 Level of C_2 contamination for T6 shot conditions

Test No.	Shock speed (m/s)	Fill pressure (Pa)	Gas comp. by volume	C_2 contamination by volume
T6s482	6200	107.541	100% N_2	0.009%
T6s478	6100	105.132	79% N_2, 21% O_2	0.02%
T6s493	7050	33.755	100% N_2	0.08%
T6s484	7300	33.287	79%N_2, 21% O_2	0.08%
T6s501	7250	33.287	79% N_2, 21% O_2	0.12%
T6s495	7250	18.235	100% N_2	0.08%
T6s491	7250	18.034	79% N_2, 21% O_2	0.08%

Test No.	Shock speed (m/s)	Fill pressure (Pa)	Gas comp. by volume	C_2 contamination by volume	Difference to synthetic radiance (no C rad.)
T6s482	6200	107.541	100% N_2	0.009%	2.0%
T6s478	6100	105.132	79% N_2, 21% O_2	0.02%	0.2%
T6s493	7050	33.755	100% N_2	0.08%	20.0%
T6s484	7300	33.287	79%N_2, 21% O_2	0.08%	0.7%
T6s501	7250	33.287	79% N_2, 21% O_2	0.12%	2.0%
T6s495	7250	18.235	100% N_2	0.08%	19.0%
T6s491	7250	18.034	79% N_2, 21% O_2	0.08%	0.8%

A. Reacting Shock-Tube Model

The Non-Equilibrium Shock Solver (NESS) was developed by Clarke et al. [23] to appropriately model reacting shock tube flows. A critical factor to consider is the mass loss to the boundary layer, a phenomenon investigated by Clarke [17] and found to be particularly pertinent in slower-reacting flows, such as those associated with the presence of radiating carbon products. NESS uses a fully compressible, reacting, quasi-one-dimensional formulation of the Navier-Stokes equations in cylindrical co-ordinates, in the shock frame of reference. This model uses the experimentally measured shock speed as an inflow boundary condition, under the assumption of a constant shock speed. The Mirels' approach is applied to characterize the radial outflow of mass [22], modelling the mass loss to the boundary layer and thus aligning the particle time of flight more closely with experimental results [17]. The formulation is completed with a stagnation boundary condition and a slug length that corresponds to Mirels' maximal length. Through the use of the compressible Navier-Stokes equations and recursive grid refinement, NESS achieves full resolution of the shock structure. These distinctive features enable NESS to integrate thermochemistry models from literature with shock tube hydrodynamics, effectively simulating shock tube experiments.

B. Thermochemistry Model

The thermochemistry model used to analyse the chosen test cases is comprised of four distinct components:

- Chemical reaction rates
- Collision cross sections
- Millikan-White values
- Electron-neutral collision cross section

Energy addition due to ionization and dissociation can be determined from the thermodynamic properties of reactants and products, with a dissociation efficiency of 0.5 used to model preferential dissociation from higher vibrational energy levels.

1. Reaction rates

The thermochemistry model used by the numerical model is a combination of 11-species synthetic air rates from Cruden et al. [13] and Park et al. [24], supplemented with rates for carbonaceous species from Park et al. [25]. A two-temperature model is utilised, with the geometric average temperature T_a utilised for dissociation reactions and the electro-vibronic temperature T_e used for electron impact reactions. The species considered in the analysis are e^-, C, N, O, C^+, N^+, O^+, CO, C_2, N_2, CN, NO, O_2, C_3, NO^+, $N_2{}^+$, and $O_2{}^+$. The list of reactions, controlling temperature T_s, reaction rate constants for the modified Arrhenius equation of form $C \times T^n \exp\left[-T_E/T_s\right]$, and sources are shown in Table 3. Backwards reaction rates are calculated using the equilibrium constant derived from the minimisation of Gibbs free energy.

2. Millikan-White Constants

The Millikan-White approach to translational-vibrational relaxation times is utilised [26]. Values for the characteristic temperature for each molecular species are shown in Table 4 and are found using the harmonic vibrational frequency found in NIST [27]. These parameters are then used to generate values usable in the Millikan and White equation for translational-vibrational relaxation time [26], using the form:

$$P\tau_{MW,ij} = \exp\left[A_{ij}(T^{-\frac{1}{3}} - b_{ij}) - 18.42\right] \tag{1}$$

Where A_{ij} and b_{ij} are specified for each interacting pair ij by:

$$A_{ij} = 0.00116\mu_{ij}^{\frac{1}{2}}\theta_i^{\frac{4}{3}} \tag{2}$$

$$b_{ij} = 0.015\mu_{ij}^{\frac{1}{4}} \tag{3}$$

Where μ is the reduced molecular mass between the two species and θ_i is the characteristic temperature of the dissociating species. Further detail regarding the summation of the relaxation times can be found in Clarke et al. [23]. These approximate values are only used where values for specific pairs are not given in Park et al. [24] .

Table 3 Reaction rates utilised during numerical analysis

Reaction	Temperature	C	n	T_E	Reference
$N_2 + M_1 \rightleftharpoons 2\,N + M_1$	T_a	7.000E+21	-1.600E+00	1.132E+05	[13]
$O_2 + M_2 \rightleftharpoons 2\,O + M_2$	T_a	2.000E+21	-1.500E+00	5.936E+04	[13]
$NO + M_3 \rightleftharpoons N + O + M_3$	T_a	1.500E+15	0.000E+00	7.457E+04	[13]
$C_2{}^+ M_4 \rightleftharpoons 2\,C + M_4$	T_a	3.700E+14	0.000E+00	6.990E+04	[25]
$CN + M_5 \rightleftharpoons C + N + M_5$	T_a	2.500E+14	0.000E+00	8.774E+04	[25]
$N_2 + e^- \rightleftharpoons 2\,N + e^-$	T_e	1.200E+07	2.690E+00	1.132E+05	[13]
$NO + e^- \rightleftharpoons N + O + e^-$	T_e	5.700E+18	0.000E+00	7.457E+04	[13]
$N + e^- \rightleftharpoons N^+ + 2\,e^-$	T_e	2.500E+34	-3.820E+00	1.686E+05	[13]
$O + e^- \rightleftharpoons O^+ + 2\,e^-$	T_e	3.900E+33	-3.780E+00	1.585E+05	[13]
$N_2 + O \rightleftharpoons NO + N$	T_t	6.400E+17	-1.000E+00	3.840E+04	[24]
$NO + O \rightleftharpoons O_2 + N$	T_t	8.400E+12	0.000E+00	1.940E+04	[24]
$O + N \rightleftharpoons NO^+ + e^-$	T_e	8.800E+08	1.000E+00	3.190E+04	[13]
$N + N \rightleftharpoons N_2{}^+ + e^-$	T_e	4.400E+07	1.500E+00	6.750E+04	[13]
$O + O \rightleftharpoons O_2{}^+ + e^-$	T_e	7.100E+02	2.700E+00	8.060E+04	[13]
$N^+ + N_2 \rightleftharpoons N_2{}^+ + N$	T_t	7.000E+06	1.470E+00	1.313E+04	[13]
$O^+ + N_2 \rightleftharpoons N_2{}^+ + O$	T_t	9.100E+11	3.600E-02	2.280E+04	[13]
$O_2{}^+ + O \rightleftharpoons O^+ + O_2$	T_t	4.000E+12	-9.000E-02	1.800E+04	[13]
$O^+ + NO \rightleftharpoons N^+ + O_2$	T_t	1.400E+05	1.900E+00	2.660E+04	[13]
$NO^+ + O_2 \rightleftharpoons O_2{}^+ + NO$	T_t	2.400E+13	4.100E-01	3.260E+04	[13]
$NO^+ + N \rightleftharpoons N_2{}^+ + O$	T_t	7.200E+13	0.000E+00	3.550E+04	[13]
$NO^+ + O \rightleftharpoons N^+ + O_2$	T_t	1.000E+12	5.000E-01	7.720E+04	[13]
$O_2{}^+ + N \rightleftharpoons N^+ + O_2$	T_t	8.700E+13	1.400E-01	2.860E+04	[13]
$O_2{}^+ + N_2 \rightleftharpoons N_2{}^+ + O_2$	T_t	9.900E+12	0.000E+00	4.070E+04	[13]
$NO^+ + N \rightleftharpoons O^+ + N_2$	T_t	3.400E+13	-1.080E+00	1.280E+04	[13]
$NO^+ + O \rightleftharpoons O_2{}^+ + N$	T_t	7.200E+12	2.900E-01	4.860E+04	[13]
$NO + N^+ \rightleftharpoons NO^+ + N$	T_t	1.800E+12	5.700E-01	0.000E+00	[13]
$C + e^- \rightleftharpoons C^+ + 2\,e^-$	T_e	3.700E+31	-3.000E+00	1.3072E+05	[25]
$CO + C \rightleftharpoons C_2 + O$	T_t	2.000E+17	-1.000E+00	5.800E+04	[25]
$CO + O \rightleftharpoons O_2 + C$	T_t	3.900E+13	-1.800E-01	6.920E+04	[25]
$CO + N \rightleftharpoons CN + O$	T_t	1.000E+14	0.000E+00	3.860E+04	[25]
$N_2 + C \rightleftharpoons CN + N$	T_t	1.100E+14	-1.100E-01	2.320E+04	[25]
$CN + O \rightleftharpoons NO + C$	T_t	1.600E+13	1.000E-01	1.460E+04	[25]
$CN^+ C \rightleftharpoons C_2 + N$	T_t	5.000E+13	0.000E+00	1.300E+04	[25]
$CO + C_2 \rightleftharpoons C_3 + O$	T_t	1.000E+12	0.000E+00	4.120E+04	[25]
$C_3 + N \rightleftharpoons CN + C_2$	T_t	1.000E+12	0.000E+00	3.420E+04	[25]
$C_3 + C \rightleftharpoons C_2 + C_2$	T_t	1.000E+12	0.000E+00	1.640E+04	[25]

Table 4 Characteristic temperatures of molecular species for use in Millikan-White approximations

Species	Characteristic Temperature (K)
N_2	3394
N_2^+	3176
O_2	2273
O_2^+	2743
NO	2620
NO^+	4159
CN	2977
CO	3123
C_2	2670
C_3	1762

3. Effective Cross-Section for Vibrational Relaxation

The model described by Equation 56 in Gnoffo et al. [28] is utilised to modify the translational-vibrational relaxation time at high temperatures, which requires a value for the effective cross-section for vibrational relaxation σ_v. The form of σ_v (in m^2) is taken from Park et al. [24].

$$\sigma_v = 3 \times 10^{-21} \left(\frac{50000}{T} \right)^2 \tag{4}$$

4. Electron-Neutral collision cross-section

Where available, electron-neutral cross sections are taken from Gnoffo et al. [28] for use in the Appleton and Bray correlation [29], used to estimate the relaxation time between translational and electronic energy modes. The remaining species are considered as trace species and thus are assumed to have a negligible impact on the energy transfer.

C. Radiance Model

NASA's NEQAIR v15.2 [30] is a line by line code developed by NASA to estimate radiance emissions, given a specified profile of temperatures and number densities. This allows the output the spatially resolved temperature and number density profile from NESS to determine the expected radiance from the numerical model. The model used by the analysis assumed a flux limited non-Boltzmann distribution with local escape factor of 1.0. This corresponds to a Line 3 input of `N F L 1.0` in the *neqair.inp* file. Experimentally determined spatial resolution functions (SRF) and instrument line shapes (ILS) convolve the NEQAIR simuluations to account for broadening mechanisms contained within the experimental setup, thus enabling comparison between the experimental and numerical results.

IV. Results

The comparison of the numerical results to experimental can be broken into three parts, the 6 km/s shots at 100 Pa, the 7km/s shots at 33 Pa and the 7 km/s shots at 18 Pa, with approximately equivalent nitrogen and synthetic air tests for each condition. The analysis herein highlights some common features in the resulting dataset, as well as highlighting results of particular note. References to blue side radiance is for the data between 200-520 nm, and red side radiance is referencing the data from wavelengths between 585 and 850 nm. CEA was used to evaluate the equilibrium composition [31], allowing a determination to be made as to how far the flow is from being fully equilibriated. The results for each test are found in Appendices A-C.

A. Carbon Contamination

Two tests particularly highlight the influence of carbon contamination on shock tube spectroscopy results, shots T6s484 and T6s501. Both tests had an approximately 7.3 km/s shock speed in 33 Pa synthetic air (71% N_2, 21% O_2 by volume) with an estimated contamination of 0.08% C_2 by volume. As we are most interested in the influence of carbon,

the blue side will be focused on due to CN radiance most significantly altering the spectra. To interrogate the presence of carbon in the flow, a nominally equivalent test (T6s501) to T6s484 was conducted with an altered spectroscopy setup to obtain high resolution data between 335 to 393 nm. For T6s484, the integrated radiance profile is reasonably well matched after 5 mm (see Figure 2a)). For T6s501, the integrated radiance profile is particularly well matched after 7 mm with the addition of C_2 (see Figure 2b)) The agreement for the decay in radiance between experimental and numerical simulations indicate the importance of utilising NESS. Mirels' effects are significant at these pressures [17], thus the time of flight effects must be modelled correctly to match the experimental results.

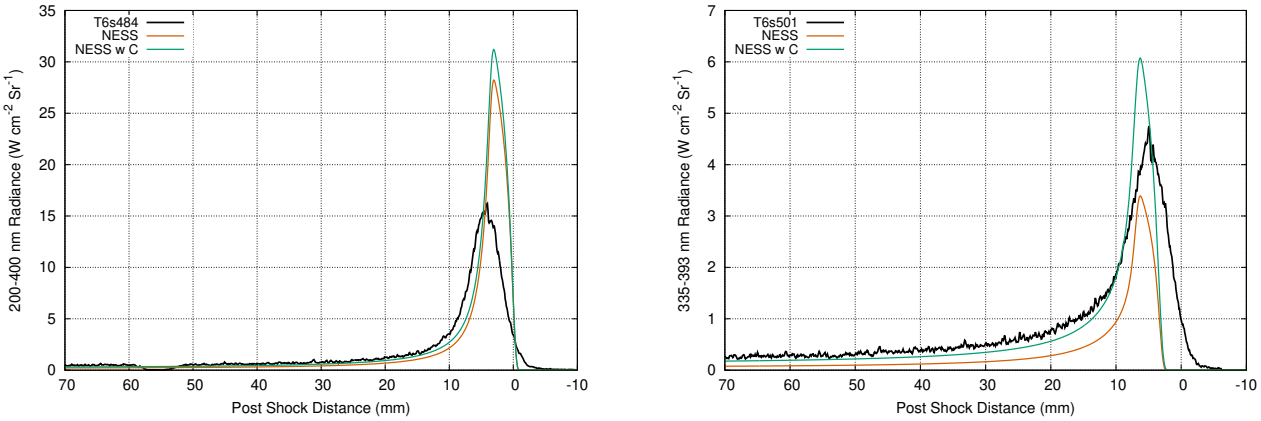

(a) T6s484 integrated radiance profile from 200-400 nm (b) T6s501 integrated radiance profile from 335 nm to 393 nm.

Fig. 2 Comparison of the numerical models for integrated radiance with the affect of carbon contamination. 7.3 km/s shock in 33 Pa synthetic air (71% N_2, 21% O_2, contamination of 0.08% C_2 by volume)

.

Examining the non-equilibrium peaks further in Figure 3a), we see an overprediction in radiance in the lower wavelength NO region. The ratio of the N_2 peaks is mostly consistent with experimental results, however the addition of CN drastically overpredicts radiance in the 380 nm region. Possible explanations include the carbon contamination varies spatially along the tube axis, such as if the carbon is being lifted off the wall and into the boundary layer. Alternatively, the carbonaceous species initially present in the core flow could be CO_2 rather than C_2, which would further delay the formation of CN due to the chemistry pathway being longer.

In comparison for T6s501 (see Figure 3b)), the non-equilibrium region is dramatically improved by the addition of carbon and the subsequent presence of CN, although the broadness of the CN region at 380 nm results in the overprediction of radiance. However the features are well matched, demonstrating the significant contribution of carbon contaminants to the overall radiance. An intriguing feature is the discrepancy in the radiance between 360-390 nm in each experiment. This further indicates the uniqueness of each experiment, and emphasises the importance of understanding the source of carbon contamination as to why this may occur.

The spectral radiance ~70 mm post shock demonstrates that the flow was close to equilibrium (see Figure 4). The addition of carbon improves agreement with experiment, however the NO region between 200-280 nm is lower than experimental values for shot T6s484, which is consistent with the higher pressure synthetic air case. The higher resolution features of the contaminated equilibrium radiance profile matches extremely well with experimental results for T6s501, although indicates the choice of 0.08% C_2 by volume was slightly lower than what was experimentally observed.

B. Modelling of the Thermal Non-Equilibrium Region

In all tests, the non-equilibrium peak radiance is overpredicted, with a typical spatially resolved integrated radiance profile being shown in Figure 5. This figure shows results from T6s482, a 6.2km/s shock in 100 Pa pure nitrogen with a chosen level of carbon contamination of 0.009% C_2 by volume. This difference in carbon contamination in the equivalent synthetic air test (0.02% C_2) is hypothesised to be due to variations in cleaning performance of the shock tube. Both the blue and red sides of the numerical model significantly overpredicts the non-equilibrium radiance, however the shape of the decay is relatively well matched from 7 mm onwards, particularly on the blue side.

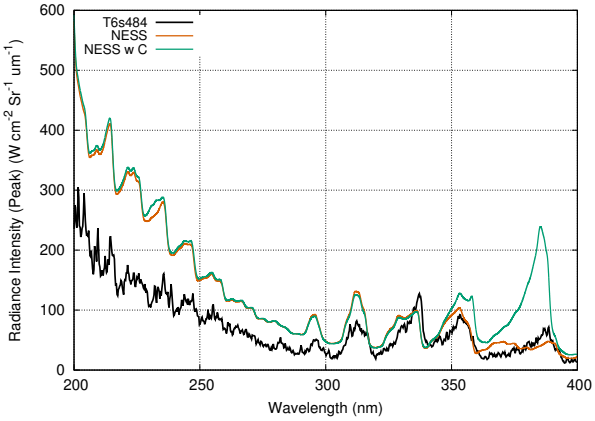

(a) Radiance profile from 200nm to 400 nm for T6s484

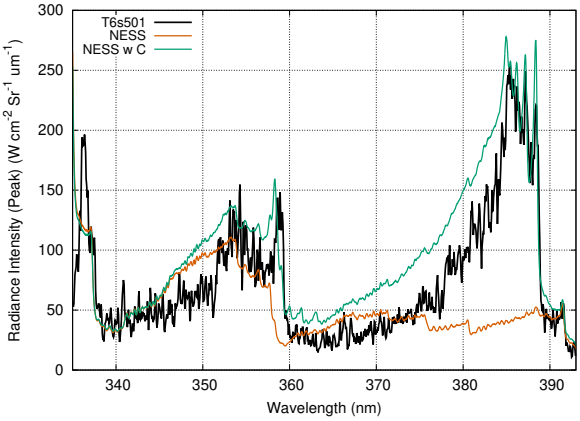

(b) Radiance profile from 335 nm to 393 nm for T6s501

Fig. 3 Assessment of the spectral distribution averaged over ± 1mm of peak radiance.7.3 km/s shock in 33 Pa synthetic air (71% N_2, 21% O_2, contamination of 0.08% C_2 by volume)

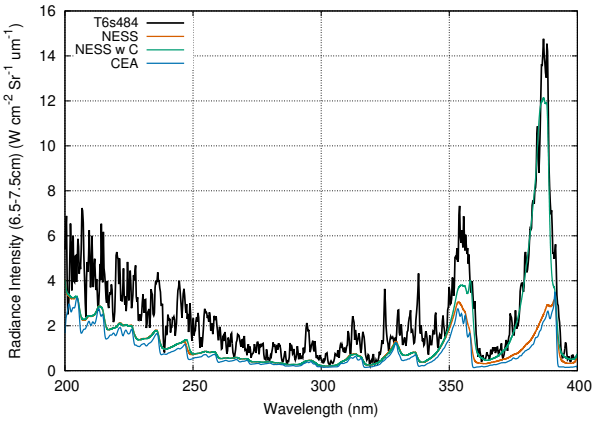

(a) Radiance profile from 200nm to 400 nm for T6s484

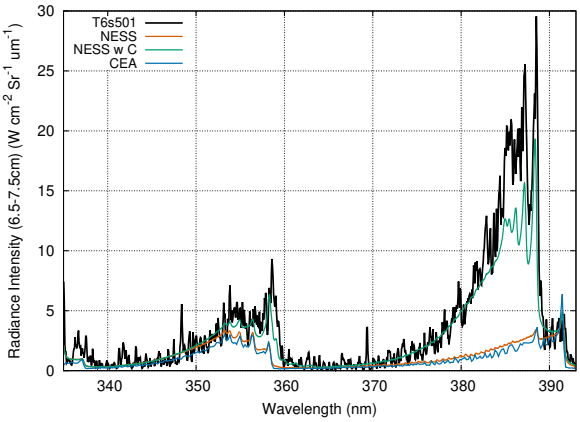

(b) Radiance profile from 335 nm to 393 nm for T6s501

Fig. 4 Comparison of the spectral distribution at ~70 mm post shock distance. 7.3 km/s shock in 33 Pa synthetic air (71% N_2, 21% O_2, contamination of 0.08% C_2 by volume)

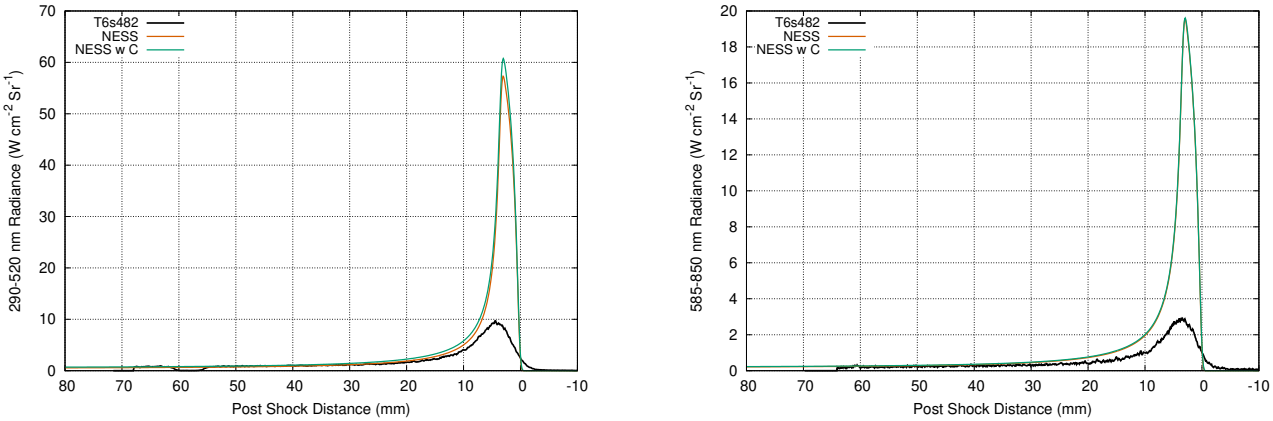

(a) Spatial radiance profile integrated from 290nm to 520 nm (b) Spatial radiance profile integrated from 585nm to 800 nm

Fig. 5 Comparison of integrated radiance profiles from T6s482, a 6.2km/s shock in 100 Pa nitrogen. Estimated contamination of 0.009% C_2 by volume.

The comparison of the spectral distribution at peak non-equilibrium is made in Figure 6, which on the blue side shows that the addition of carbon slightly better matches the shape of the peak in radiance around 380 nm (due to $CN_{\Delta v=0}$).

However, the ratio of the peak radiance at approximately 310 nm compared to 380 nm is significantly higher for the numerical results compared to experimental. This gives an indication of issues with the prediction of the vibrational temperature profile, as NEQAIR is predicting an overpopulation of N_2 at the state corresponding to this wavelength. The overall magnitude of both red and blue spectra is significantly overpredicted by the numerical model, possibly indicating the relaxation times between energy modes may not be representative and thus not resolving the temperature profiles appropriately in the thermal non-equilibrium region.

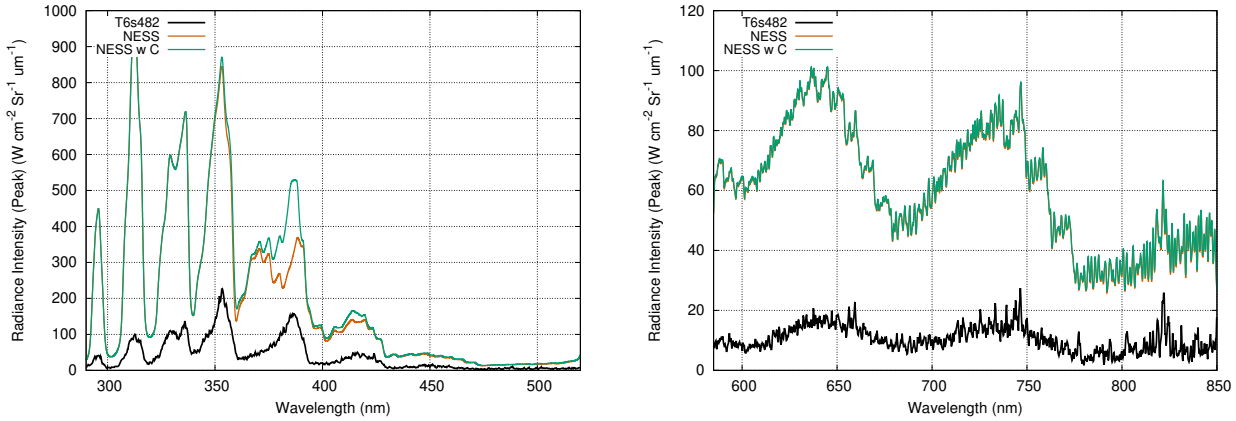

(a) Radiance profile from 290 nm to 520 nm (b) Radiance profile from 585nm to 800 nm

Fig. 6 Assesment of the spectral distribution averaged over ± 1mm of peak radiance for T6s482. Estimated contamination of 0.009% C_2 by volume.

C. Hydrogen Contaminants and Modelling of Atomic Oxygen

Test T6s491 is a 7.25 km/s shock in 18 Pa synthetic air modelled with an estimated contamination of 0.08% C_2 by volume. This is the best fit to the experimental radiance for both red and blue sides, with the addition of carbon further improving the fit (see Figure 7).

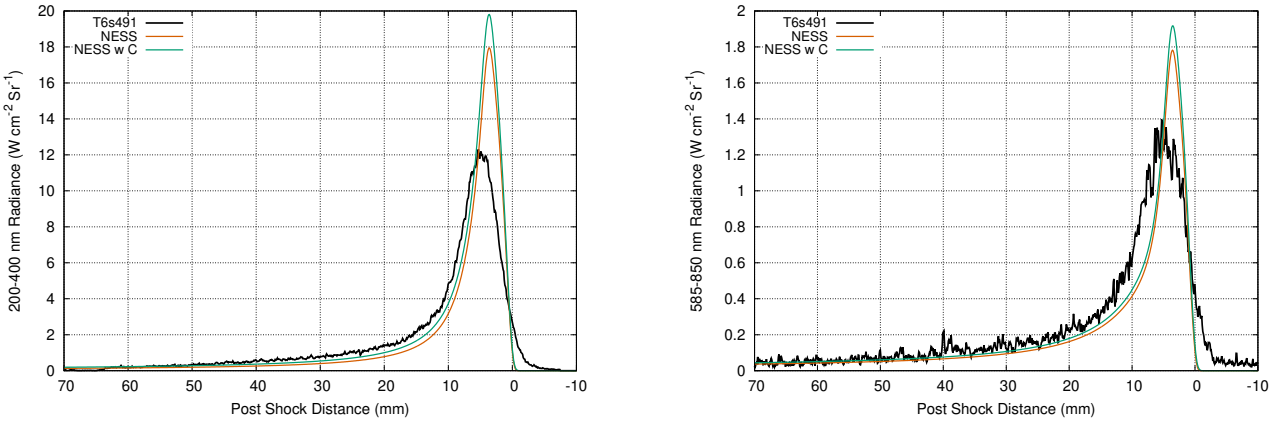

(a) Spatial radiance profile integrated from 200nm to 400 nm (b) Spatial radiance profile integrated from 585nm to 800 nm

Fig. 7 Comparison of integrated radiance profiles from T6s491, a 7.25km/s shock in 18 Pa synthetic air. Estimated contamination of 0.08% C_2 by volume.

The spectra at the non-equilibrium peak (see Figure 8) offer some interesting insight into issues with both the numerical model and sources of additional flow contamination. At wavelengths less than 300 nm, the discrepancy between experiment and numerical prediction increase, indicating issues in the reaction rates associated with NO, which is consistent with the analysis of Cruden et al. [13]. The amount of radiance produced by atomic oxygen (777 nm) is significantly lower than experimentally observed, indicating the lack of atomic oxygen in the flow. This could be attributed to the consumption of atomic oxgen in the formation of NO, as well as due to the dissociation rate of O_2 being lower than required. Two features common in the synthetic air shots are visible in the non-equilibrium spectra, the peak at 656 nm and the sharp spike overlaid onto the N_2 peak at approximately 330 nm. The 656 nm peak corresponds to the presence of H – α and the 330 nm region could correspond to the presence of NH. The H – α feature is present in the non-equilibrium region of most tests, with the NH feature also clearly visible in T6s484. These features indicate the presence of hydrogen contamination, possibly due to the presence of water contamination.

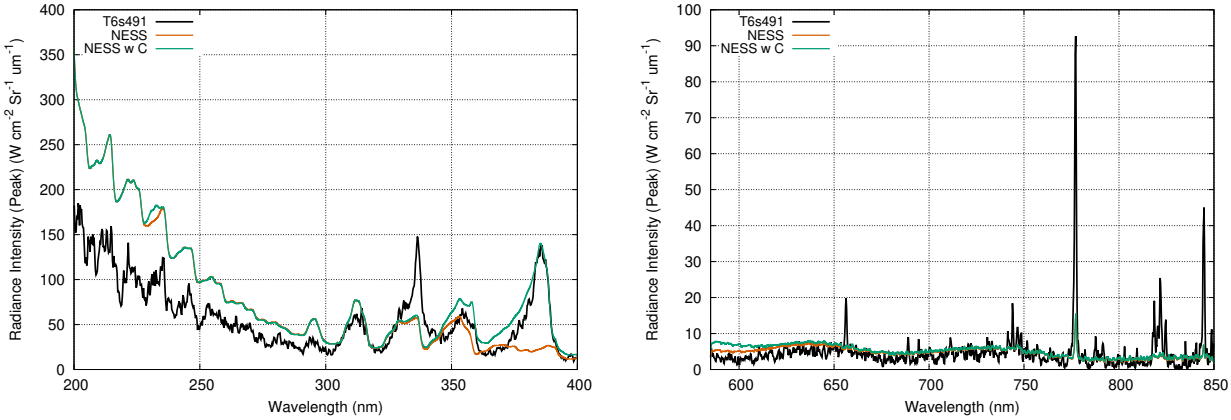

(a) Radiance profile from 200nm to 400 nm (b) Radiance profile from 585nm to 800 nm

Fig. 8 Comparison of spectral distributions averaged over ± 1mm of peak radiance for T6s491, a 7.25km/s shock in 18 Pa synthetic air. Estimated contamination of 0.08% C_2 by volume.

D. Influence of Carbon Contamination on Thermochemistry

A key question for this paper is the influence of carbon on the thermochemistry of the numerical model, specifically the temperature profiles and the species number densities. Test T6s493, a 7km/s shock in 33 Pa pure nitrogen shot with an estimated contamination of 0.08% C_2 by volume, provides an indication of this for the thermochemistry model used by this paper. Once again, the peak integrated radiance is overpredicted in the non-equilibrium region, however the decay matches reasonably well from 10 mm onwards (see Figure 9).

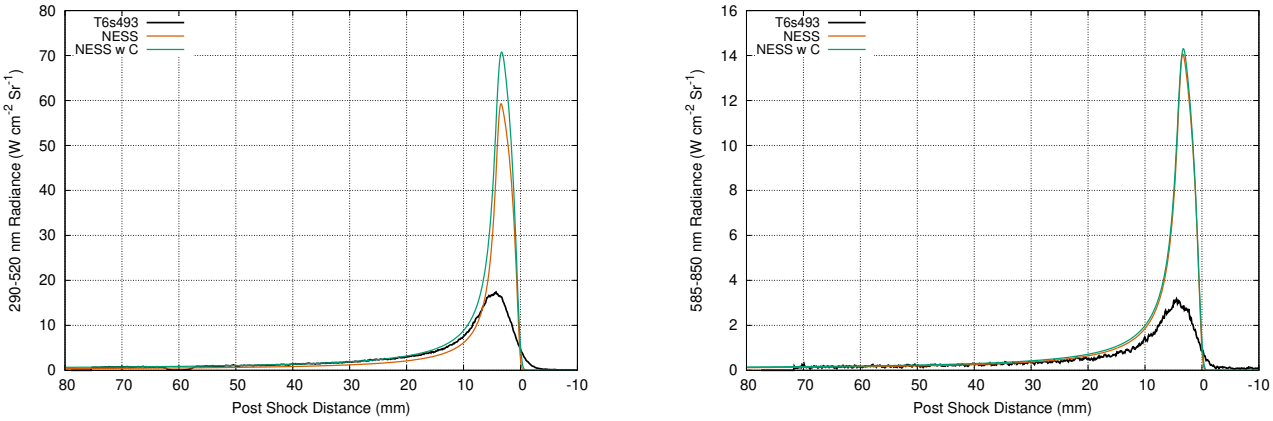

(a) Spatial radiance profile integrated from 290nm to 520 nm (b) Spatial radiance profile integrated from 585nm to 800 nm

Fig. 9 Assessment of radiance profiles from T6s493, a 7.05 km/s shock in 33 Pa nitrogen. Estimated contamination of 0.08% C_2 by volume.

This approximately corresponds to the location of equilibriation between thermal modes (see Figure 10), indicating the spatially resolved state properties from the numerical model are close to experimental values from this point onwards. The discrepancy between temperature profiles is negliglible, with the peak temperature difference of 1% occurring at the location of peak translational temperature.

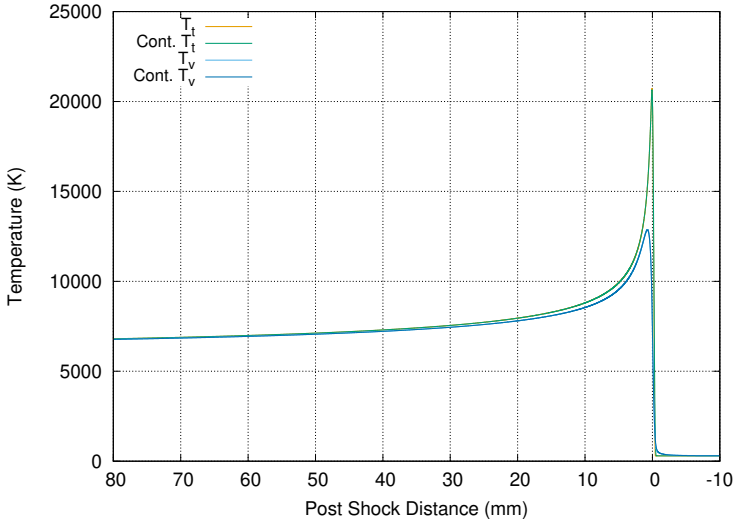

Fig. 10 Temperature profiles from T6s493.

The spectra at ~70 mm post shock distance is very well modelled (see Figure 11), even though the flow still has significant relaxation to occur before reaching equilibrium. The addition of C_2 into the fill gas composition greatly improves the match to experimental radiance at lower wavelengths, due to the presence of CN radiance. This

demonstrates the importance of appropriately modelling the time of flight characteristics of the flow, justifying the use of a dedicated shock tube solver.

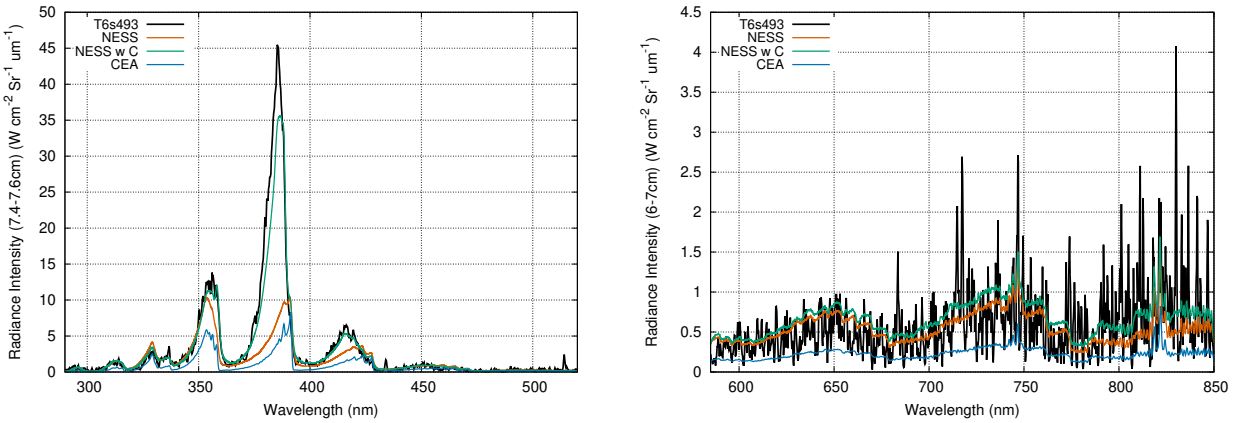

(a) Radiance profile from 290nm to 520 nm

(b) Radiance profile from 585nm to 800 nm

Fig. 11 Spectral distribution at ~70 mm post shock distance for T6s493, a 7.05 km/s shock in 33 Pa nitrogen. Estimated contamination of 0.08% C_2 by volume.

The addition of carbon seems to have a small affect on the atomic emission between 585 and 850 nm, due to an increase in electrons in the flow due to the presence of C^+ (see Figure 12). Temperatures and neutral species number densities are minimally changed, which results in the similar radiance profile at lower wavelengths in areas unaffected by CN radiance. This indicates that for this thermochemistry model, the radiance is a superposition of the carbonaceous species with the uncontaminated fill gas flow properties. This may not hold for higher speeds where increased ionization may occur.

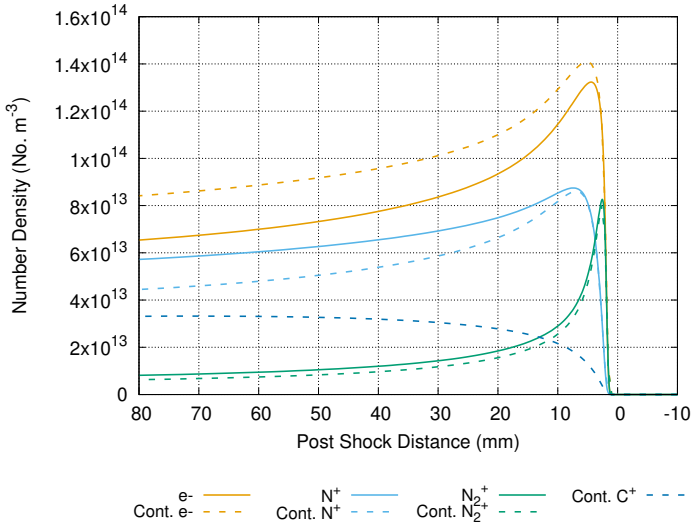

Fig. 12 Charged product number densities from NESS, showing the difference due to contaminants. Dashed lines are from the NESS simulations with carbon contamination present

V. Conclusion

A variety of shock tube experiments ranging from shock speeds of 6 to 7.3 km/s propagating through fill pressures ranging from 18 to 100 Pa were simulated using a quasi-one dimensional numerical tool specifically developed for

simulation of reacting gas flows in shock tubes. A two-temperature thermochemistry model was tested using this tool, which allowed the influence of carbon contamination in shock tubes to be investigated. The addition of carbon contaminants does not significantly affect the temperature profiles nor the molecular species present in the flow, but did slightly increase the number density of charged species. Therefore, spectra associated with molecular features is a superposition of the synthetic air species with the carbonaceous species, specifically CN. This significantly improved the estimation of radiance in the non-equilibrium and equilibrium regions, particularly due to the radiance from CN. Caution must be taken in extrapolating this result to other thermochemistry models, or outside of the range of fill pressures and shock speeds analysed in this paper.

The non-equilibrium region radiance was consistently overpredicted by the model, in particular overpredicting the NO region and not matching the ratios of the N_2 peaks. The non-equilibrium radiance from O is underpredicted, which could be attributed to overconsumption by the production of NO and/or insufficient dissociation of O_2. The presence of $H-\alpha$ and NH in the non-equilibrium region indicates hydrogen also contaminates shock tube flow, although not always as visible as carbon contamination and potentially arises due to the presence of water vapour. The shape of the decay was well modelled in the cases considered, indicating NESS appropriately modelled the time of flight effects via consideration of the influence of mass loss to the boundary layer. The equilibrium region was well predicted by including carbon contaminants, although the NO region is consistently underpredicted. Future work could consider the presence of hydrogen in the fill gas via the presence of water vapour, as well as including CO_2 as a possible source of contamination. Rates involving the dissociation of O_2 and the formation of NO should be examined against experimental data, as well as by changing the parameters governing the relaxation of energy between energy modes.

Appendix

A. 6km/s Shock in 100 Pa Test Gas

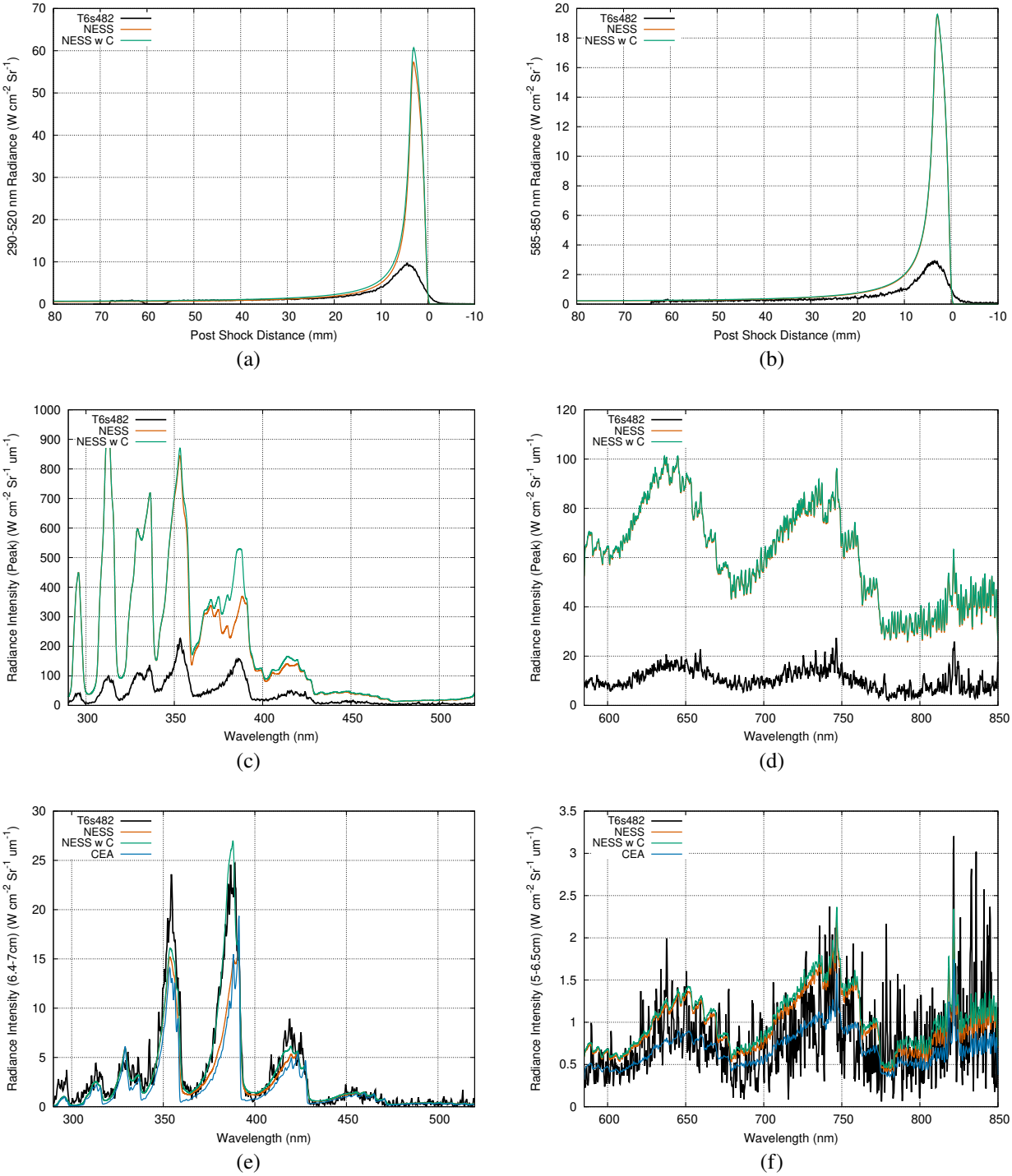

Fig. 13 Radiance profiles from T6s482, a 6.2km/s shock in 100 Pa nitrogen. Estimated carbon contamination of 0.009% C_2 contamination by volume. Spatial radiance profile integrated from (a) 290nm to 520 nm, and (b) 585nm to 800 nm. Spectral distributions averaged over ± 1mm of peak radiance (c) from 290nm to 520 nm, and (d) 585nm to 800 nm. Spectral distributions averaged ~70 mm post shock distance from (e) 290 nm to 520 nm, and (f) 585nm to 800 nm

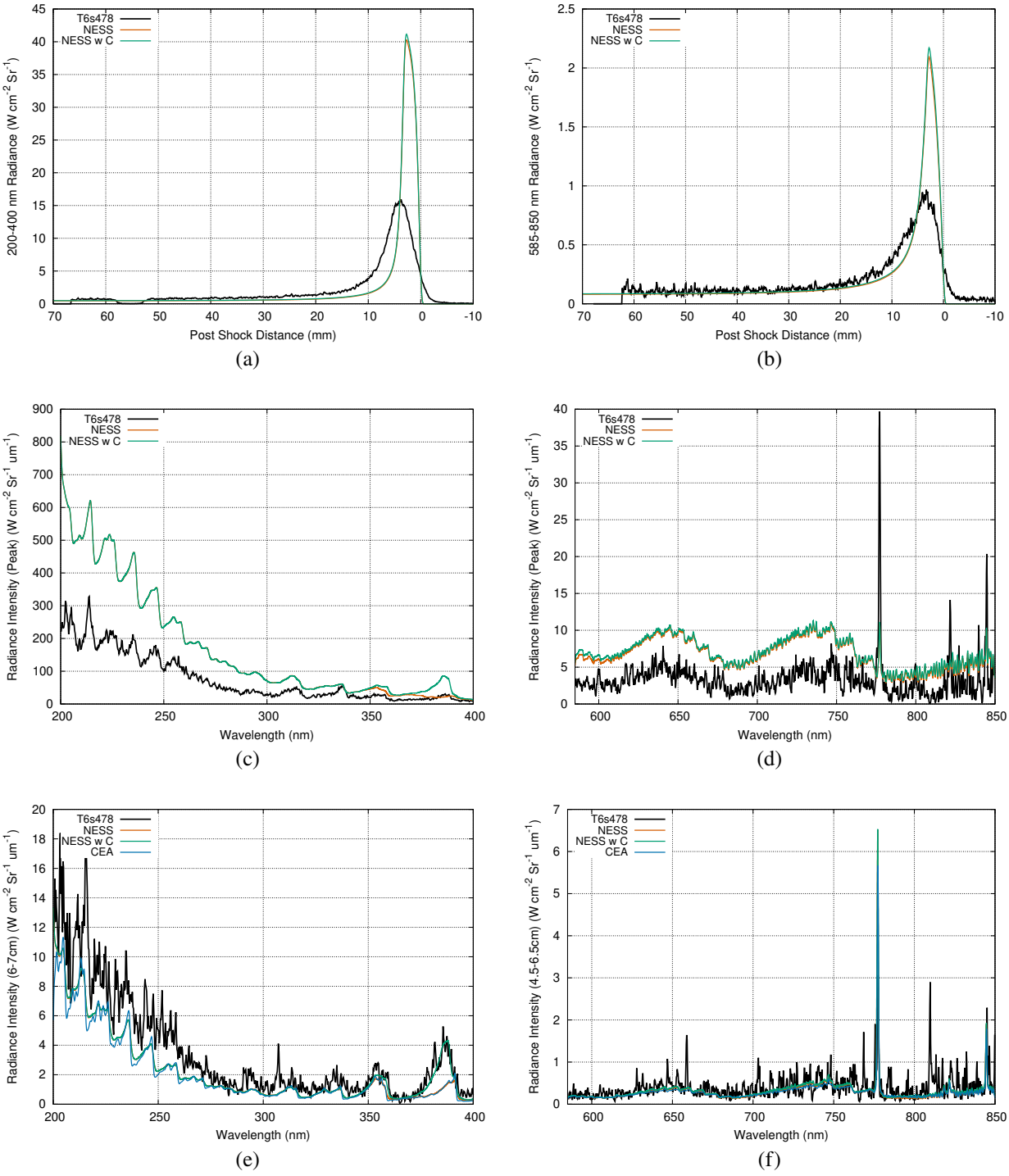

Fig. 14 Radiance profiles from T6s478, a 6.1km/s shock in 100 Pa synthetic air (79% N_2, 21% O_2 by volume). Estimated carbon contamination of 0.02% C_2 contamination by volume. Spatial radiance profile integrated from (a) 200 nm to 400 nm, and (b) 585nm to 800 nm. Spectral distributions averaged over ± 1mm of peak radiance (c) from 200nm to 400 nm, and (d) 585nm to 800 nm. Spectral distributions averaged ~70 mm post shock distance from (e) 200 nm to 400 nm, and (f) 585nm to 800 nm

B. 7km/s Shock in 33 Pa Test Gas

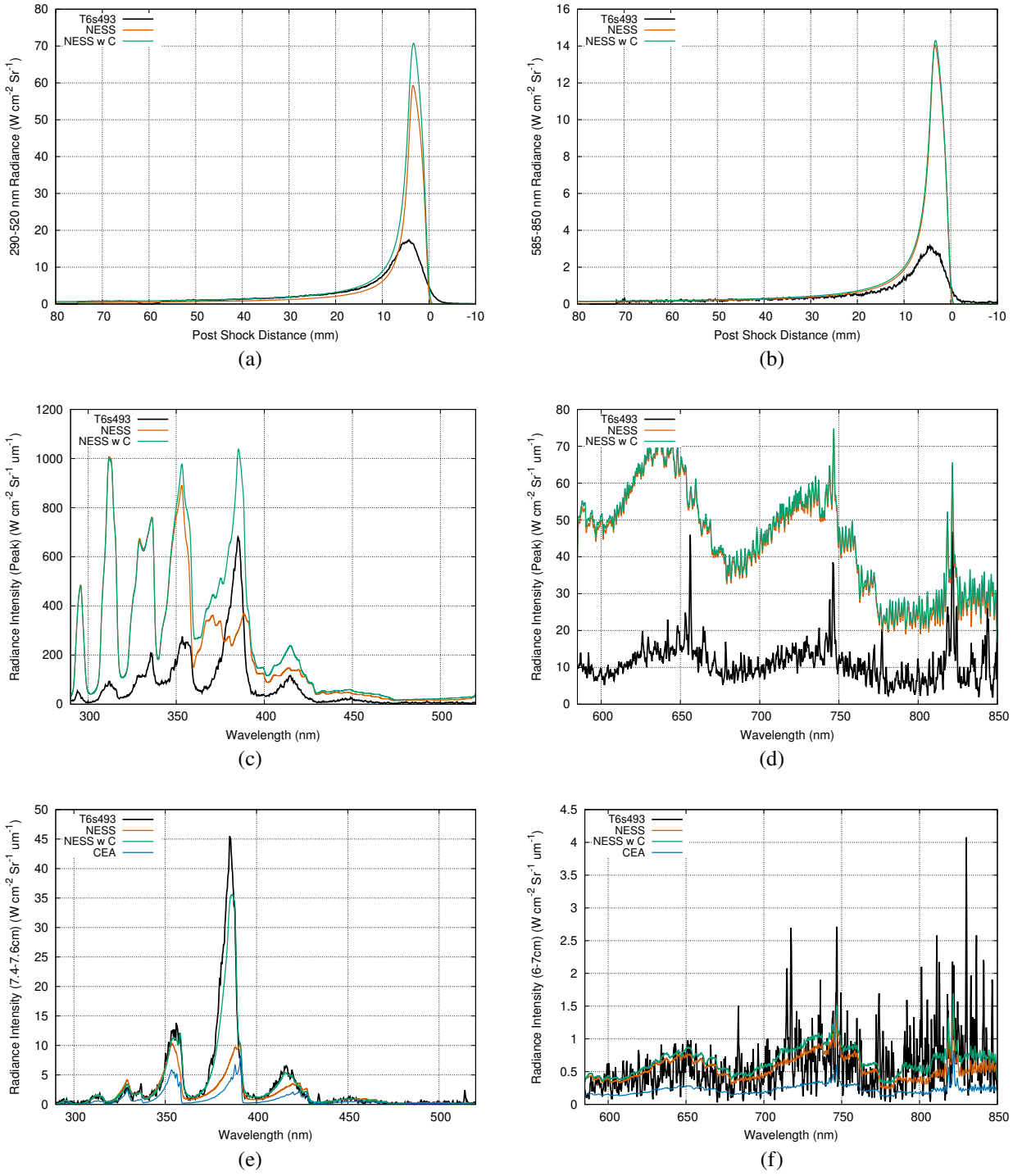

Fig. 15 Radiance profiles from T6s493, a 7.05km/s shock in 33 Pa nitrogen. Estimated carbon contamination of 0.08% C_2 contamination by volume. Spatial radiance profile integrated from (a) 290nm to 520 nm, and (b) 585nm to 800 nm. Spectral distributions averaged over ± 1mm of peak radiance (c) from 290nm to 520 nm, and (d) 585nm to 800 nm. Spectral distributions averaged ~70 mm post shock distance from (e) 290 nm to 520 nm, and (f) 585nm to 800 nm

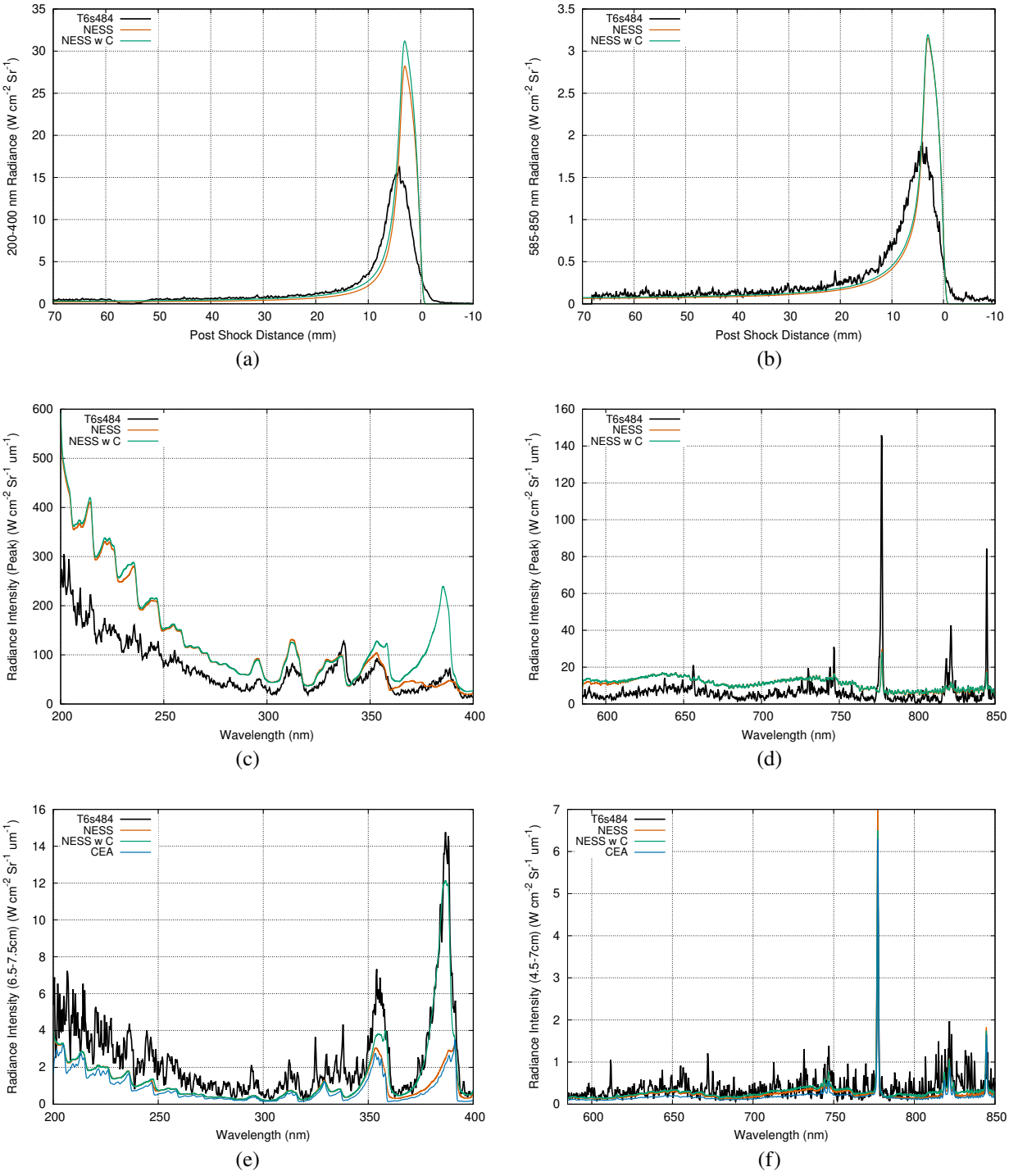

Fig. 16 Radiance profiles from T6s484, a 7.3 km/s shock in 33 Pa synthetic air (79% N_2, 21% O_2 by volume). Estimated carbon contamination of 0.02% C_2 contamination by volume. Spatial radiance profile integrated from (a) 200 nm to 400 nm, and (b) 585nm to 800 nm. Spectral distributions averaged over ± 1mm of peak radiance (c) from 200nm to 400 nm, and (d) 585nm to 800 nm. Spectral distributions averaged ~70 mm post shock distance from (e) 200 nm to 400 nm, and (f) 585nm to 800 nm

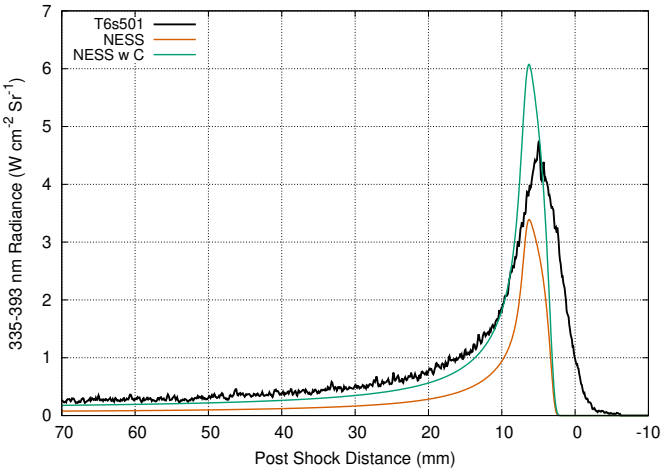

(a)

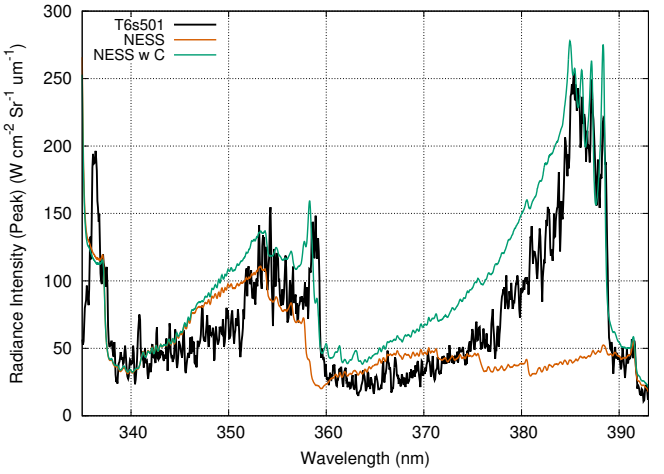

(b)

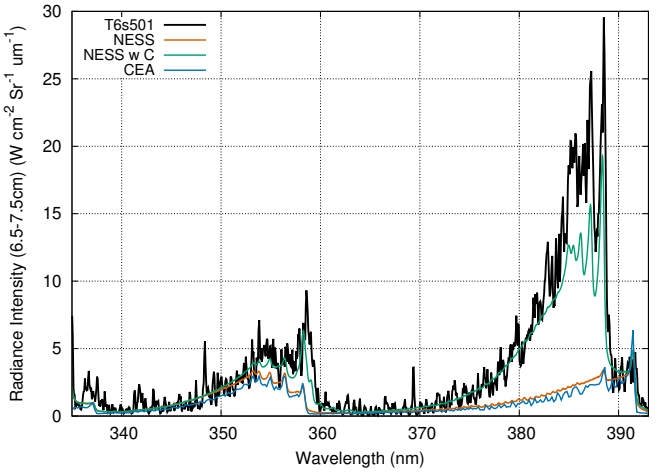

(c)

Fig. 17 Radiance profiles from T6s501, a 7.25km/s shock in 33 Pa synthetic air. Estimated carbon contamination of 0.02% C_2 contamination by volume. Spatial radiance profile integrated integrated from (a) 335nm to 393 nm. Spectral distribution averaged over ± 1mm of peak radiance from (b) 335nm to 393 nm. Spectral distribution averaged ~70 mm post shock distance from (c) 335nm to 393 nm

C. 7km/s Shock in 18 Pa Test Gas

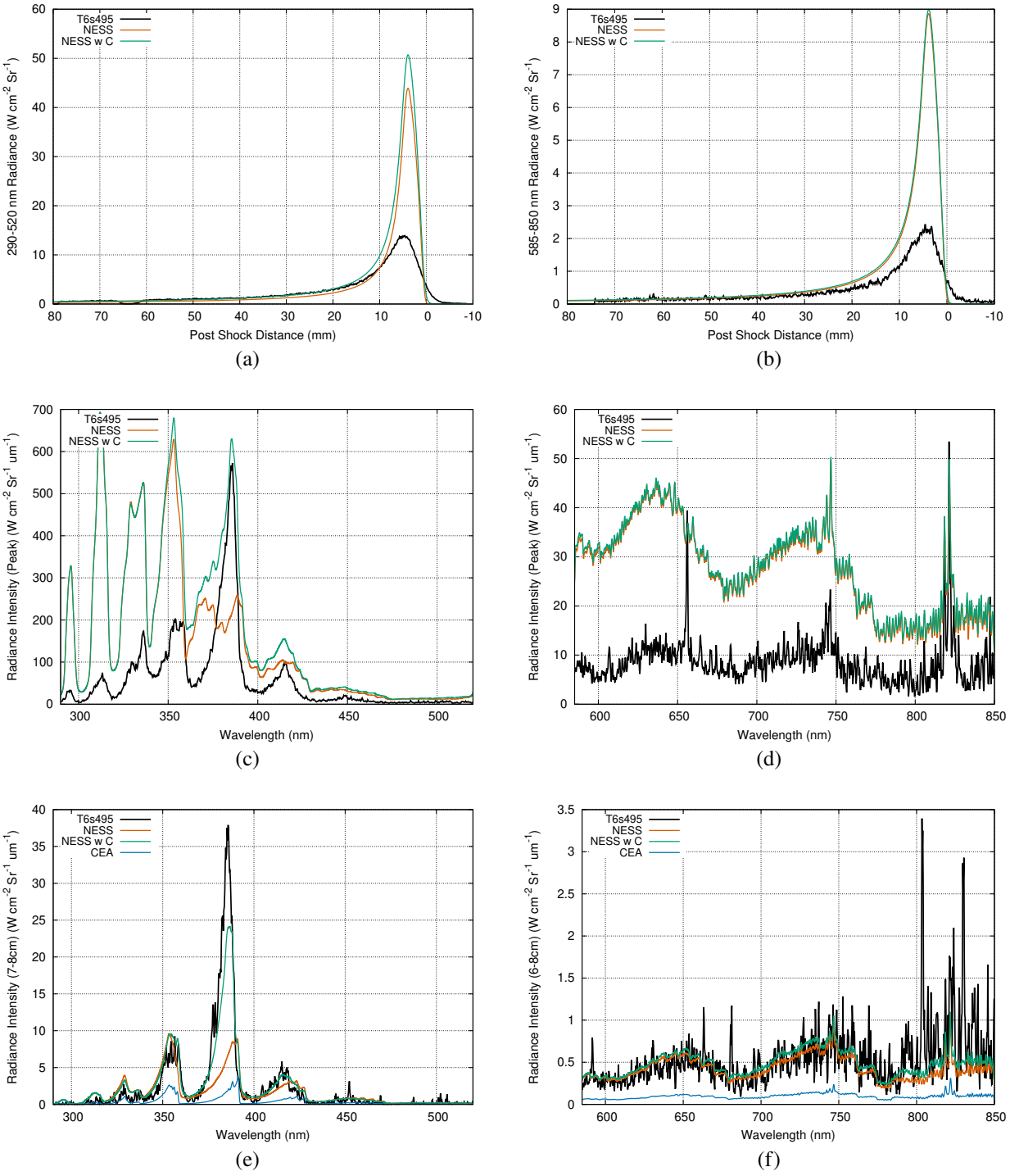

Fig. 18 Radiance profiles from T6s495, a 7.25km/s shock in 18 Pa nitrogen. Estimated carbon contamination of 0.08% C_2 contamination by volume. Spatial radiance profile integrated from (a) 290nm to 520 nm, and (b) 585nm to 800 nm. Spectral distributions averaged over ± 1mm of peak radiance (c) from 290nm to 520 nm, and (d) 585nm to 800 nm. Spectral distributions averaged ~70 mm post shock distance from (e) 290 nm to 520 nm, and (f) 585nm to 800 nm

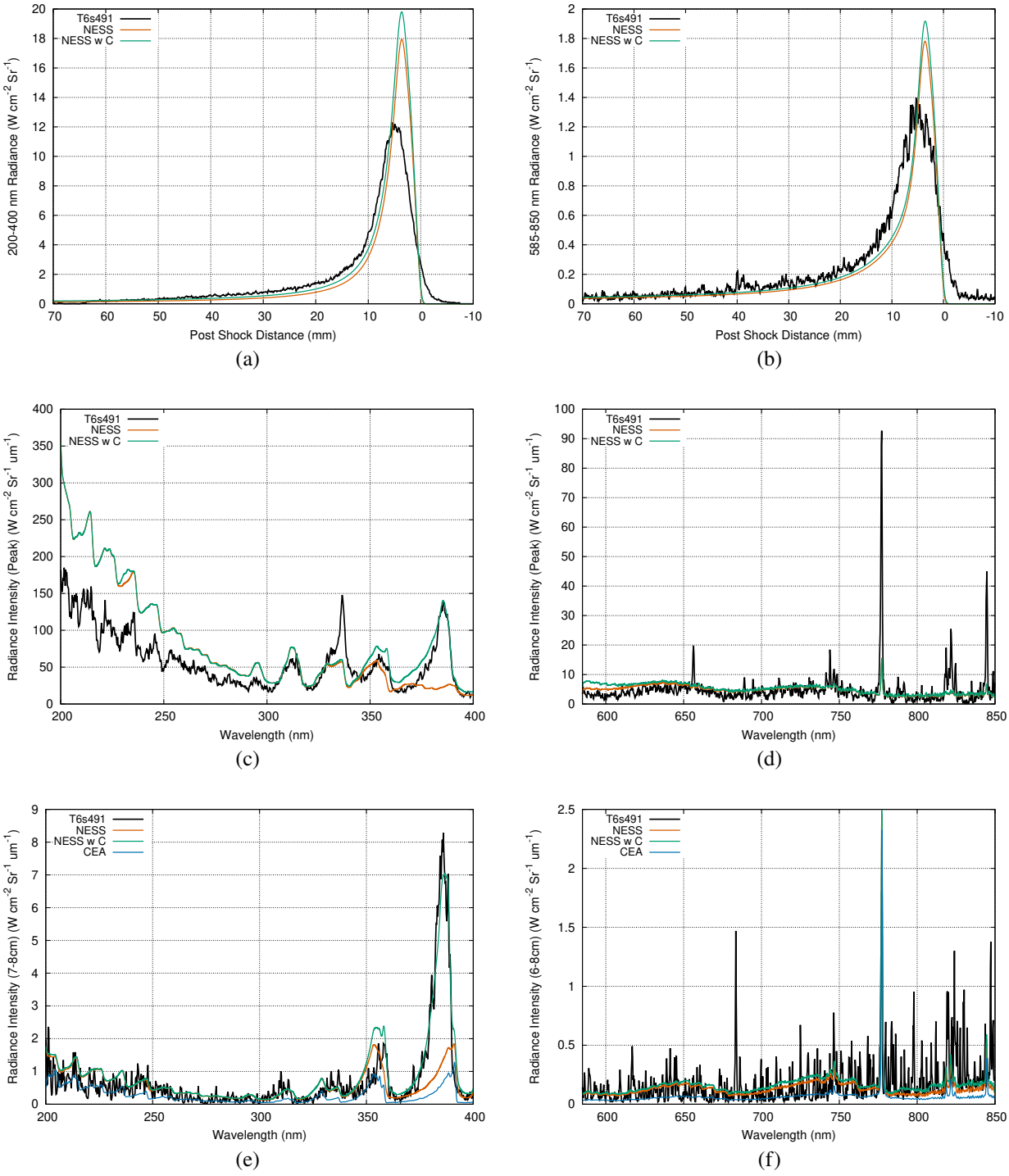

Fig. 19 Radiance profiles from T6s491, a 7.25 km/s shock in 18 Pa synthetic air (79% N_2, 21% O_2 by volume). Estimated carbon contamination of 0.02% C_2 contamination by volume. Spatial radiance profile integrated from (a) 200 nm to 400 nm, and (b) 585nm to 800 nm. Spectral distributions averaged over ± 1mm of peak radiance (c) from 200nm to 400 nm, and (d) 585nm to 800 nm. Spectral distributions averaged ~70 mm post shock distance from (e) 200 nm to 400 nm, and (f) 585nm to 800 nm

Acknowledgements

We would like to acknowledge the funding of Justin Clarke's DPhil by the Rhodes Trust.

References

[1] Park, C., *Nonequilibrium Hypersonic Aerothermodynamics*, Wiley, New York, 1990.

[2] Collen, P., Doherty, L. J., Subiah, S. D., Sopek, T., Jahn, I., Gildfind, D., Penty Geraets, R., Gollan, R., Hambidge, C., Morgan, R., and McGilvray, M., "Development and commissioning of the T6 Stalker Tunnel," *Experiments in Fluids*, Vol. 62, No. 11, 2021, p. 225. https://doi.org/10.1007/s00348-021-03298-1, URL https://link.springer.com/10.1007/s00348-021-03298-1.

[3] McGilvray, M., Dann, A. G., and Jacobs, P. A., "Modelling the complete operation of a free-piston shock tunnel for a low enthalpy condition," *Shock Waves*, Vol. 23, No. 4, 2013, pp. 399–406. https://doi.org/10.1007/s00193-013-0437-8.

[4] Simpson, C. J., Chandler, T. R., and Bridgman, K. B., "Effect on shock trajectory of the opening time of diaphragms in a shock tube," *Physics of Fluids*, Vol. 10, No. 9, 1967, pp. 1894–1896. https://doi.org/10.1063/1.1762384.

[5] Rothkopf, E. M., and Low, W., "Diaphragm opening process in shock tubes," *Physics of Fluids*, Vol. 17, No. 6, 1974, pp. 1169–1173. https://doi.org/10.1063/1.1694860.

[6] Mirels, H., "Attenuation in a shock tube due to unsteady-boundary-layer action," Tech. rep., 1957.

[7] Satchell, M., Collen, P., McGilvray, M., and Di Mare, L., "Numerical simulation of shock tubes using shock tracking in an overset formulation," *Aiaa Aviation 2020 Forum*, Vol. 1, 2020, pp. 1–22. https://doi.org/10.2514/6.2020-2722.

[8] Freedman, E., and Daiber, J. W., "Decomposition Rate of Nitric Oxide Between 3000 and 4300°K," *The Journal of Chemical Physics*, Vol. 34, No. 4, 1961, pp. 1271–1278. https://doi.org/10.1063/1.1731731.

[9] Dunn, M. G., and Lordi, J. A., "Measurement of $O_2^+ + e^-$ Dissociative Recombination in Expanding Oxygen Flows," *AIAA Journal*, Vol. 8, No. 4, 1970, pp. 614–618. https://doi.org/10.2514/3.5730.

[10] Byron, S., *Interferometric Measurement in a Shock Tube of Dissociation Rates for Air and its Component Gases*, Cornell University, New York, 1959.

[11] Park, C., "Two-temperature interpretation of dissociation rate data for N_2 and O_2," *26th Aerospace Sciences Meeting*, American Institute of Aeronautics and Astronautics, 1988. https://doi.org/10.2514/6.1988-458, URL https://arc.aiaa.org/doi/10.2514/6.1988-458.

[12] Glenn, A. B., Collen, P. L., and McGilvray, M., "Radiation Measurements of Shockwaves in Synthetic Air and Pure Nitrogen," *AIAA Science and Technology Forum and Exposition, AIAA SciTech Forum 2024*, 2024.

[13] Cruden, B. A., and Brandis, A. M., "Measurement of Radiative Non-equilibrium for Air Shocks Between 7-9 km/s," *47th AIAA Thermophysics Conference*, American Institute of Aeronautics and Astronautics, Reston, Virginia, 2017, pp. 1–36. https://doi.org/10.2514/6.2017-4535, URL https://arc.aiaa.org/doi/10.2514/6.2017-4535.

[14] Cruden, B. A., and Brandis, A. M., "Measurement of radiative nonequilibrium for air shocks between 7 and 9 km/s," *Journal of Thermophysics and Heat Transfer*, Vol. 34, No. 1, 2020, pp. 154–180. https://doi.org/10.2514/1.T5735.

[15] Glenn, A. B., Collen, P. L., and McGilvray, M., "Experimental Non-Equilibrium Radiation Measurements for Low-Earth Orbit Return," *AIAA Science and Technology Forum and Exposition, AIAA SciTech Forum 2022*, 2022. https://doi.org/10.2514/6.2022-2154.

[16] Brandis, A. M., and Cruden, B. A., "Titan atmospheric entry radiative heating," *47th AIAA Thermophysics Conference, 2017*, 2017, pp. 1–27. https://doi.org/10.2514/6.2017-4534.

[17] Clarke, J., Di Mare, L., and McGilvray, M., "Spatial Transformations for Reacting Gas Shock Tube Experiments," *AIAA Journal*, Vol. 61, No. 8, 2023, pp. 1–10. https://doi.org/10.2514/1.j062604, URL https://arc.aiaa.org/doi/10.2514/1.J062604.

[18] Tibère-Inglesse, A. C., West, T. K., Jelloian, C. C., Minesi, N. Q., Spearrin, R. M., Clarke, J., Di Mare, L., McGilvray, M., and Cruden, B. A., "Examination of Mars2020 shock-layer conditions via infrared emission spectroscopy of CO2," *AIAA SCITECH 2023 Forum*, American Institute of Aeronautics and Astronautics, Reston, Virginia, 2023, pp. 1–20. https://doi.org/10.2514/6.2023-0960, URL https://arc.aiaa.org/doi/10.2514/6.2023-0960.

[19] Collen, P. L., Di Mare, L., McGilvray, M., and Satchell, M., "Analysis of Shock Deceleration Effects on Radiation Experiments in the NASA Electric Arc Shock Tube." *AIAA Science and Technology Forum and Exposition, AIAA SciTech Forum 2022*, 2022. https://doi.org/10.2514/6.2022-0267.

[20] Satchell, M., di Mare, L., and McGilvray, M., "Flow Nonuniformities Behind Accelerating and Decelerating Shock Waves in Shock Tubes," *AIAA Journal*, Vol. 60, No. 3, 2022, pp. 1537–1548. https://doi.org/10.2514/1.J060375.

[21] Collen, P. L., Satchell, M., Di Mare, L., and McGilvray, M., "The influence of shock speed variation on radiation and thermochemistry experiments in shock tubes," *Journal of Fluid Mechanics*, Vol. 948, 2022, p. A51. https://doi.org/10.1017/jfm.2022.727.

[22] Mirels, H., "Test time in low-pressure shock tubes," *Physics of Fluids*, Vol. 6, No. 9, 1963, pp. 1201–1214. https://doi.org/10.1063/1.1706887.

[23] Clarke, J., Di Mare, L., and McGilvray, M., "Quasi One-Dimensional Non-Equilibrium Shock Tube Solver," *Submitted to AIAA Journal*, 2024.

[24] Park, C., "Review of chemical-kinetic problems of future NASA missions, I: Earth entries," *Journal of Thermophysics and Heat Transfer*, Vol. 7, No. 3, 1993, pp. 385–398. https://doi.org/10.2514/3.431.

[25] Park, C., Jaffe, R. L., and Partridge, H., "Chemical-kinetic parameters of hyperbolic earth entry," *38th Aerospace Sciences Meeting and Exhibit*, Vol. 15, No. 1, 2000. https://doi.org/10.2514/6.2000-210.

[26] Millikan, R. C., and White, D. R., "Systematics of vibrational relaxation," *The Journal of Chemical Physics*, Vol. 39, No. 12, 1963, pp. 3209–3213. https://doi.org/10.1063/1.1734182.

[27] NIST, "Experimental Vibrational Frequencies," , 2022. Data retrieved from Computational Chemistry Comparison and Benchmark DataBase, https://cccbdb.nist.gov/expvibs1x.asp.

[28] Gnoffo, P. A., Gupta, R. N., and Shinn, J. L., "Conservation Equations and Physical Models for Hypersonic Air Flows in Thermal and Chemical Nonequilibrium," Tech. Rep. NASA-TP-2867, NASA, 1989.

[29] Appleton, J. P., and Bray, K. N., "The conservation equations for a non-equilibrium plasma," *Journal of Fluid Mechanics*, Vol. 20, No. 4, 1964, pp. 659–672. https://doi.org/10.1017/S0022112064001458.

[30] Whiting, E. E., Chul, P., Liu, Y., Arnold, O., and Paterson, A., "NEQAIR96, Nonequilibrium and Equilibrium Radiative Transport and Spectra Program: User's Manual," Tech. Rep. December, NASA, 1996.

[31] Gordon, S., and McBride, B. J., "Computer Program for Calculation of Complex Chemical Equilibrium," Tech. Rep. NASA-RP-1311, 1994.